RSC Advances

ROYAL SOCIETY OF CHEMISTRY

www.rsc.org/advances

Journal Name

RSCPublishing

ARTICLE

Composition-Tuned $Sn_xGe_{1-x}S$ Nanocrystals for Enhanced-Performance Lithium Ion Batteries

Cite this: DOI: 10.1039/x0xx00000x

Young Rok Lim, [a] Hyung Soon Im, [a] Yong Jae Cho, [a] Jeunghee Park,[a]* Eun Hee Cha,[b]* and Won Il Cho[c]*

Received 00th January 2012,
Accepted 00th January 2012

DOI: 10.1039/x0xx00000x

www.rsc.org/

Germanium- or tin-based nanostructures have recently demonstrated outstanding lithium ion storage ability and are considered to be the most promising candidates to substitute current carbonaceous anodes in lithium ion batteries. Tin germanium sulfide ($Sn_xGe_{1-x}S$) ternary alloy nanocrystals (NCs) were synthesized by a gas-phase laser photolysis reaction with complete composition control ($0 \le x \le 1$). All of these composition-tuned nanocrystals showed excellent cycling performances in lithium ion batteries. Reversible capacities were in the range 800–1200 mAh/g after 70 cycles, which is close to the theoretical capacities of each composition. As the tin composition (x) was increased, the rate capability greatly enhanced. This unique composition dependence of the electrochemical properties was explained by the lower charge transfer resistance due to the high conductivity of $Sn_xGe_{1-x}S$ NCs as well as Sn_xGe_{1-x} alloy NCs produced upon lithiation. Sn-rich $Sn_xGe_{1-x}S$ NCs are, therefore, promising candidates for applications in high-performance energy conversion systems.

Introduction

Germanium (Ge) and Tin (Sn) are considered to be the most promising candidates as alternative materials to substitute commercial carbonaceous anodes in lithium ion batteries (LIBs).[1-4] Their bulk phases are known to have higher theoretical capacities, 1620 mAh/g for Ge and 990 mAh/g for Sn, than graphite carbon (370 mAh/g) owing to Li alloy formation (*i.e.*, $Li_{22}Ge_5$ and $Li_{22}Sn_5$). However, large volume changes (up to 300%) during lithiation/delithiation induce pulverization and mechanical stress diminishing the electrical interface contact, which leads to capacity fading in bulk electrodes. Recently, a number of papers have shown that the use of sulfide nanostructures can reduce this degradation by mitigating the volume-change stress.[5-25] Sulfide compounds such as GeS and SnS are irreversibly converted to Ge or Sn in the first cycle: GeS (or SnS) + $2Li^+ + 2e^- \rightarrow$ Ge (or Sn) + Li_2S. Subsequently, Ge (or Sn) can efficiently store and release Li^+ ions inside the amorphous Li_2S buffer matrix according to the reversible alloying/dealloying reaction expressed by Ge (or Sn) + $xLi^+ + xe^- \leftrightarrow Li_xGe$ or Li_xSn ($0 \le x \le 4.4$). During this substantial lithiation/delithiation process, Ge (or Sn) works as the active material and Li_2S as the inert matrix surrounding the active Ge (or Sn) nanocrystals (NCs) suppressing the electrode failure caused by volume change. In addition, a size reduction to the nanoscale, which results in an increase in the surface/volume ratio, can minimize the volume change and dissipate mechanical stress. Our group has already demonstrated the excellent cycling performance of these materials; reversible capacities are 1220 mAh/g for GeS NCs and 880 mAh/g for SnS NCs after 70-100 cycles.[6,7,24]

Herein, we investigate the cycling performance of $Sn_xGe_{1-x}S$ ternary composition alloy NCs in LIBs. The NCs were synthesized with complete composition control over the range $0 \le x \le 1$ by a gas-phase laser photolysis reaction of appropriate precursors ($Sn(CH_3)_4$, $Ge(CH_3)_4$, and H_2S). GeS and SnS have gained popularity in photon energy harvesting applications because of their relatively higher chemical and environmental stability than the more toxic chalcogenides (e.g., PbS).[26-34] They are native *p*-type semiconductors with high absorption coefficients and narrow band gaps; E_g (bulk) = 1.5–1.6 and 1.1–1.2 eV for GeS and SnS, respectively. Previously, we reported the $Sn_xGe_{1-x}S$ NCs show remarkably higher photoconversion efficiencies in photovoltaic and photodetector devices than the end members.[34] To the best of our knowledge, few cases have so far been reported on the electrochemical properties of these alloy NCs in LIBs. We report here the synergic performance of the alloy NCs in comparison to their binary counterparts.

Experimental

Laser photolysis of ($Ge(CH_3)_4$, TMG), tetramethyl tin ($Sn(CH_3)_4$, TMT), and hydrogen sulfide (H_2S) was performed using an Nd:YAG pulsed laser (Coherent) operated at 1064 nm, with a repetition rate of 10 Hz and a pulse width of 10 ns. All the precursors were purchased from Sigma-Aldrich Co. The precursors were degassed by several freeze (77 K)-pump-thaw cycles, and used without further purification. In the typical process, the precursor vapors (< 100 Torr) were introduced to a Pyrex glass reactor, equipped with a gas valve connected to a vacuum line and a quartz optical window. The laser beam was focused into the reactor through the quartz window, by using a lens of focal length 10 cm. The experiment was carried out using the photon energy of 0.2 J/pulse. After 1 h of laser irradiation, the gas products were vented out. Subsequently, the NCs were collected by dispersing them in ethanol, followed by

evaporation and vacuum drying at room temperature. In order to obtain the crystalline phase, the obtained NC powders were thermally annealed in a quartz tube under vacuum at 300–400 °C for 1 h.

The products were characterized by scanning electron microscopy (SEM, Hitachi S-4700), field-emission transmission electron microscopy (FE TEM, FEI TECNAI G2 200 kV and Jeol JEM 2100F), high-voltage transmission electron microscopy (HVEM, Jeol JEM ARM 1300S, 1.25 MV), and energy-dispersive X-ray fluorescence spectroscopy (EDX). Fast Fourier-transform (FFT) images were generated by the inversion of the TEM images using Digital Micrograph GMS1.4 software (Gatan Inc.). High-resolution XRD patterns were obtained using the 9B and 3D beam lines of the Pohang Light Source (PLS) with monochromatic radiation. XRD measurement was also carried out in a Rigaku D/MAX-2500 V/PC using Cu Kα radiation (λ = 1.54056 Å).

For electrochemical tests, the electrodes of battery test cells were made of the active material (NCs), super P, and polyacrylic acid (PAA, 35 wt% dissolved in water; Aldrich) binder at a weight ratio of 6:2:2. The ratio of 8:1:1 or 6:2:2 gave the best results in the capacity and the stability. The tap density is avg. 0.2 g/cm^3, and the thickness of film is 150 μm. The distilled water-mixed slurry was coated onto the 20-μm-thick Cu foil. The coated electrode was dried at 80 °C for 12 h and then roll-pressed. The coin-type half cells (CR2032) were prepared in a helium-filled glove box. The cell consisted of an electrode (containing active material), Li metal, micro-porous polyethylene separator, and electrolyte solution of 1 M $LiPF_6$ in 1:1:1 volume % of ethylene carbonate (EC):ethyl methyl carbonate (EMC):dimethyl carbonate (DMC). The performance of the cells was examined using a battery testing system (Maccor 4000) at a current density of 0.1C-20C between 0.01 and 1.5 V. We usually fabricated 3~5 cells for each composition, and took the data that represent the average value. Cyclic voltammetry (CV) measurements were conducted (Biology SAS) using a voltage range of 0.01–2.5 V at a rate of 0.1 mV/s. Electrochemical impedance spectroscopy (Solartron Multistat) was carried out by applying an AC voltage of 5 mV in the frequency range of 100 kHz to 0.01 Hz. For *ex situ* XRD measurements, the charged or discharged cells were disassembled, and the electrodes were rinsed thoroughly with a DMC solution and dried in a glove box.

Results and discussion

Table S1 (ESI†) summarizes the partial pressures of the precursors used in the preparation of all the NCs (8 samples in total). The NCs exhibit a size distribution of 5–30 nm with an average diameter of 10±3 nm (Fig. 1a). Inset shows the lattice-resolved images of orthorhombic phase $Sn_{0.4}Ge_{0.6}S$ NC. The *d*-spacing of the (110) planes is estimated to be 4.0 Å, which is consistent with the value calculated by Vegard's rule using the bulk values $d_{SnS(110)}$=4.04 Å and $d_{GeS(110)}$=3.97 Å. The EDX data of individual NC reveal the feasible composition tuning between the GeS (x = 0) and the SnS (x = 1). The EDX Sn (L shell), Ge (L shell), and S (K shell) peaks show correctly a composition of x = 0, 0.4, 0.6, 0.8, and 1 (Fig. 1b). The ratio of ([Sn]+[Ge])/[S] is nearly equal to 1 for all compositions.

Fig. 2a shows the XRD patterns of the $Sn_xGe_{1-x}S$ NCs. The peaks are assigned to those of the orthorhombic GeS (JCPDS No. 85-1114, a = 4.290 Å, b = 10.42 Å, c = 3.640 Å) and SnS (JCPDS No. 39-0354; a = 4.329 Å, b = 11.19 Å, c = 3.983 Å) phases with a *Pbmn* space group. The (101), (111), and (040) peaks are displayed over a magnified scale in Fig 2b. As x increases, the peak position shifts continuously from the GeS phase to the SnS phase. The peak shift of (111) was guided by the arrows. The composition (x) of the alloy NCs was determined using Vegard's law (*i.e.*, $d = (1- x)d_{GeS} + xd_{SnS}$) based on the peak positions of the end members.

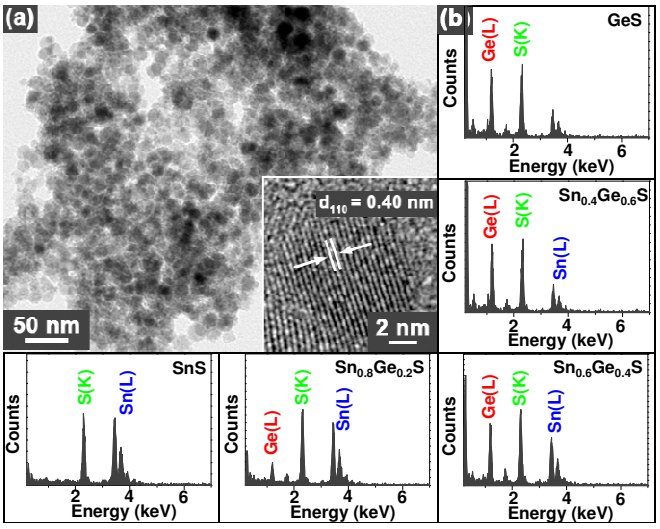

Fig. 1 (a) HRTEM image revealing the spherical shape of $Sn_{0.4}Ge_{0.6}S$ NCs. The average diameter is 10 nm. Lattice-resolved a of selected orthorhombic phase NCs shows d_{110} = 4.0 Å (inset). (b) EDX spectrum showing the composition of x = 0, 0.4, 0.6, 0.8, and 1.

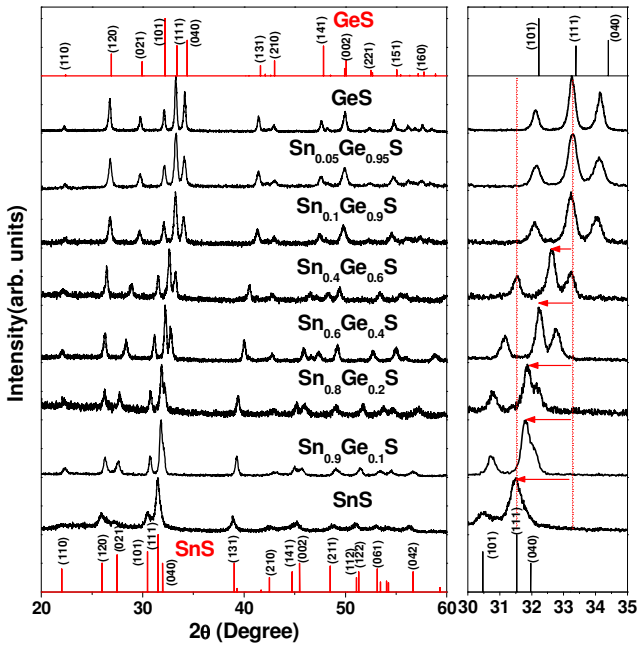

Fig. 2 (a) Full-range XRD pattern of $Sn_xGe_{1-x}S$ (x = 0, 0.05, 0.1, 0.4, 0.6, 0.8, 0.9, and 1). The peaks of GeS and SnS are indexed to the orthorhombic phases of GeS (top; JCPDS No. 85-1114, a = 4.290 Å, b = 10.42 Å, c = 3.640 Å) and SnS (bottom; JCPDS No. 39-0354; a = 4.329 Å, b = 11.19 Å, c = 3.983 Å). (b) Magnified (101), (111), and (040) peaks. The (111) peak shift upon the composition tuning was guided by the arrows.

XRD peak analysis reveals a unique anisotropic bowing phenomena of the lattice constants (ESI†, Fig. S1).[34] The lattice

constants *a* and *b* are larger than their linear values in Sn-rich compositions, while *c* shows a deviation in the opposite direction. The maximum positive deviations of the unit cell volume from the linear values occur at x = 0.8–0.9. UV-visible absorption spectra (ESI†, Fig. S2) show a non-linear dependence of E_g on the composition, which deviates from the linear value, predicted using Vegard's law. This optical bowing correlates with the bowing observed for the lattice constants. The band gap of samples when x = 0.8–0.9 is 1.2 eV, which is lower than that of SnS (1.25 eV). Since the electrical conductivity usually increases with decreasing the band gap, the electrical conductivity of alloy NCs would be maximized at this composition. Furthermore, alloy NCs with this composition have been previously observed to have the highest photoconversion efficiency in photovoltaic devices.[34] This unique composition dependence is consistent with the observed cycling performance in LIBs, as shown below.

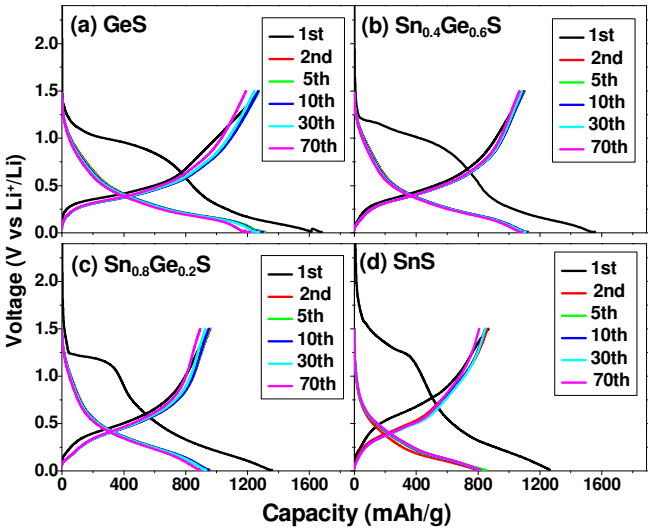

Fig. 3 Discharge–charge voltage profiles of coin-type half-cells using $Sn_xGe_{1-x}S$ NCs, where (a) x = 0, (b) x = 0.4, (c) x = 0.8, and (d) x =1, for 1, 2, 5, 10, 30, and 70 cycles tested between 0.01 and 1.5 V at a rate of 0.1C.

The electrochemical properties of all of these composition-tuned $Sn_xGe_{1-x}S$ NCs, acting as anode materials in LIBs, were examined. For convenience, we define 1C as the theoretical capacity of pure Ge (where 1C = 1620 mAh/g). Figs. 3(a)-(d) show the voltage profiles of coin-type half-cells prepared using x = 0 (GeS), 0.4 ($Sn_{0.4}Ge_{0.6}S$), 0.8 ($Sn_{0.8}Ge_{0.2}S$), and 1 (SnS) NCs for 1, 2, 5, 10, 30, and 70 cycles at a discharge/charge rate (current rate, C rate) of 0.1C, tested between 0.01 and 1.5 V. The first discharge and charge capacities of GeS are 1680 and 1273 mAh/g, respectively, with an initial coulombic efficiency of 76%. The first discharge/charge capacities of $Sn_{0.4}Ge_{0.6}S$, $Sn_{0.8}Ge_{0.2}S$, and SnS NCs are 1556/1100, 1415/962, and 1264/861 mAh/g, respectively, and the initial coulombic efficiencies are 71%, 68%, and 68%. After the first cycle, all these NCs exhibit complete capacity reversibility with an average coulombic efficiency of 97% for up to 70 cycles. The results are summarized in Table 1.

The large initial capacity loss observed can be partly attributed to the formation of solid electrolyte interphase (SEI) layers on the electrode surface during Li insertion. All NCs exhibit a plateau at approximately 1-1.2 V in the first discharge process, which is ascribed to the irreversible decomposition of the $Sn_xGe_{1-x}S$ into Sn_xGe_{1-x} and Li_2S as follows: $Sn_xGe_{1-x}S + 2Li^+ + 2e^- \rightarrow Sn_xGe_{1-x} + Li_2S$. A plateau region at approximately 0.2 V is seen for all discharge cycles and corresponds to the Li insertion process $Sn_xGe_{1-x} + xLi^+ + xe^- \rightarrow Li_xSn_xGe_{1-x}$. Cyclic voltammetry curves and the differential plots of discharge – charge voltage profiles confirm this observation with a corresponding reduction-oxidation peak pair, as shown in Figs. S3 and S4 (ESI†).

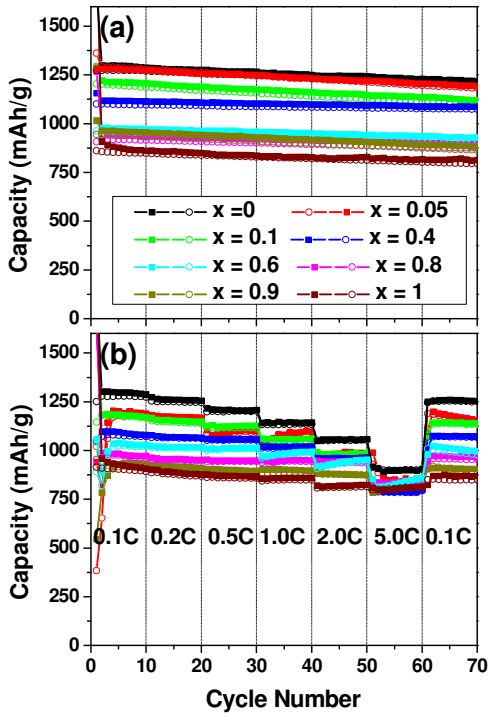

Fig. 4 (a) Discharge–charge capacity *versus* cycle number for half-cells using $Sn_xGe_{1-x}S$ (x = 0, 0.05, 0.1, 0.4, 0.6, 0.8, 0.9, and 1) NCs cycled with a rate of 0.1 C. (b) Cycling performance as the C rate is increased from 0.1C to 5.0C. The discharge and charge capacities are marked by the filled squares and hollow circles, respectively.

Fig. 4a shows the discharge/charge capacities of $Sn_xGe_{1-x}S$ (x = 0, 0.1, 0.4, 0.6, 0.8, 0.9, and 1) NCs as a function of the cycle number up to 70 cycles at a discharge/charge rate (C rate) of 0.1C. All samples exhibit very stable capacities and high coulombic efficiencies after the first cycle, indicating a perfectly reversible alloying/dealloying reaction as follows: $Sn_xGe_{1-x} + xLi^+ + xe^- \leftrightarrow Li_xSn_xGe_{1-x}$. The respective discharge capacities are 1219, 1194, 1122, 1087, 929, 894, 880, and 816 mAh/g, after 70 cycles. We assumed that Sn_xGe_{1-x} in $Sn_xGe_{1-x}S$ is only active element for lithiation/delithiation, and form $Li_{22}(Sn_xGe_{1-x})_5$ (= 4.4 Li per Sn_xGe_{1-x}). Then, theoretical capacity (mAh/g) is 4.4×26800 mAh/g. For GeS and SnS, where molecular weight is 104.71 and 150.78 g/mol, respectively, theoretical capacity (C_{GeS} and C_{SnS}) is 1126 and 782 mAh/g. The theoretical capacity of each composition was calculated using the equation $C(x) = (1 - x)C_{GeS} + xC_{SnS}$, where C_{GeS} = 1126 mAh/g and C_{SnS} = 782 mAh/g. The

respective theoretical capacities are 1092, 988, 920, 851, 810, and 816 mAh/g, for x = 0.05, 0.1, 0.4, 0.6, 0.8, and 0.9, respectively. The discharge capacities at 70 cycles reached an average as high as ~100% of the theoretical capacity. The composition-dependent capacities are summarized in Table 1.

The rate capability and stability were compared for each composition by gradually increasing the C rate step-wise from 0.1C to 5.0C, and then returning back to 0.1C. Fig. 4b displays the discharge/charge capacities as the C rate changes by steps of 0.1C → 0.2C → 0.5C → 1.0C → 2.0C → 5.0C → 0.1C. For each C rate, 10 discharge/charge cycles were performed. As the C rate reaches 5.0C, the capacities decrease to 898, 840, 814, 790, 828, 839, 810, and 802 mAh/g, respectively, for x = 0, 0.05, 0.1, 0.4, 0.6, 0.8, 0.9, and 1 (see also Table 2). This corresponds to an average 85% retention of the initial capacities at 0.1C (5th cycle). When the C rate is returned back to 0.1C after the 60th cycle, the capacity returns efficiently to an average 97% of the initial capacity obtained at 0.1C. A remarkable finding is that the higher Sn compositions exhibit the higher rate capability.

In order to see clearly the composition-dependent rate capability, the retention (%) of the initial discharge capacities (0.1C, 5th cycle) at the C rates of 0.5C (25th cycle), 1C (35th cycle), 2C (45th cycle), 5C (55th cycle), and 0.1C (65th cycle) *versus* the Sn composition (x) are plotted in Fig. 5. As the quantity of incorporated Sn increases, the retention of the initial discharge capacity at the higher C rates (2C and 5C) enhanced with an average value of 90%. It is obvious that the higher Sn composition enhances the rate capability.

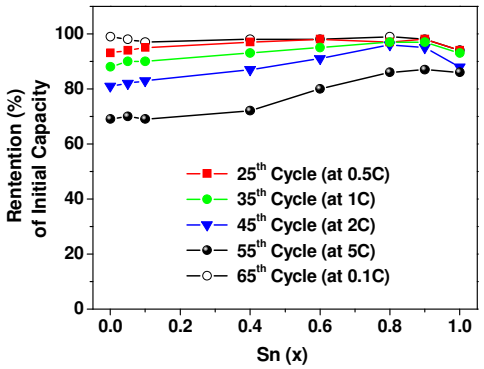

Fig. 5 Retention (%) of the initial discharge capacity (0.1C, 5th cycle) for the rate of 0.5C (25th cycle), 1C (35th cycle), 2C (45th cycle), 5C (55th cycle), and 0.1C (65th cycle)

As we discussed earlier, the Sn-rich alloy NCs exhibit high photoconductivity that usually increases along with the electrical conductivity. This increased electrical conductivity can significantly improve the kinetics of lithiation/delithiation processes and result in higher capacities. This is because as the current density (C rate) increases electron transport becomes the limiting step in the kinetics. Therefore, the greater rate capability observed when x increased could be correlated with this composition's higher electrical conductivity.

Table 1 Summary of half-cell capacities (mAh/g) using $Sn_xGe_{1-x}S$ NCs during cycles at a rate of 0.1C.

No.	x(Sn)	Theoretical capacity	First cycle			70th cycle	
			discharge	charge	η(%)[a]	discharge	η(%) for 5-70 cycles
1	0	1126	1680	1273	76	1219	97.8
2	0.05	1109	1668	1246	75	1194	97.6
3	0.1	1092	1695	1204	71	1122	98.3
4	0.4	988	1556	1100	71	1087	94.1
5	0.6	920	1415	962	68	929	97.7
6	0.8	851	1358	907	67	894	97.0
7	0.9	816	1287	838	65	880	98.0
8	1	782	1264	861	68	816	96.2

[a] η = Coulomb efficiency.

Table 2 Summary of half-cell discharge capacities using $Sn_xGe_{1-x}S$ NCs at different C rates. The values in parentheses correspond to the retention (%) of the initial capacities at 0.1C (5th cycle).

No.	x (Sn)	Discharge Capacity (mAh/g)					
		0.1C (5th cycle)	0.5C (25th cycle)	1C (35th cycle)	2C (45th cycle)	5C (55th cycle)	0.1C (65th cycle)
1	0	1298	1210	1143 (88 %)	1056 (81 %)	898 (69 %)	1260 (99 %)
2	0.05	1200	1128 (94%)	1080 (90 %)	984 (82 %)	840 (70 %)	1180 (98 %)
3	0.1	1179	1125 (95 %)	1058 (90 %)	982 (83 %)	814 (69 %)	1145 (97 %)
4	0.4	1095	1057 (97 %)	1020 (93 %)	960 (87 %)	790 (72 %)	1073 (98 %)
5	0.6	1038	1013 (98 %)	986 (95 %)	939 (91 %)	828 (80 %)	1013 (98 %)
6	0.8	984	950 (97 %)	950 (97 %)	945 (96 %)	839 (86 %)	972 (99 %)
7	0.9	931	901 (97 %)	903 (97 %)	880 (95 %)	810 (87 %)	910 (98 %)
8	1	928	870 (94 %)	860 (93 %)	820 (88 %)	802 (86 %)	874 (94 %)

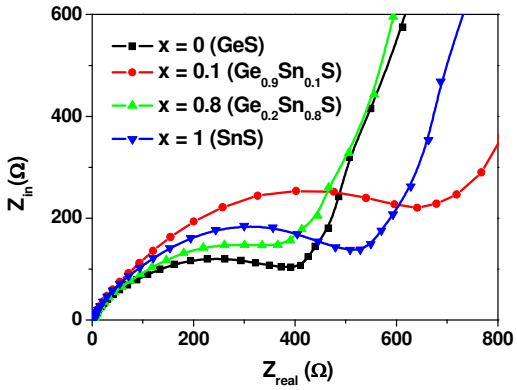

Fig. 6 Nyquist plots of $Sn_xGe_{1-x}S$ NCs, where x = 0, 0.1, 0.8, and 1.

Fig. 6 shows the Nyquist plots of compositions x = 0, 0.1, 0.8, and 1 (before the cycling test). All of the plots consist of one semicircle in the high frequency region and a straight line in the low frequency region. The semicircle portion is related to the reaction at the electrode/electrolyte interface and reflects the charge transfer impedances. Therefore the diameter of semicircle is attributed to the charge transfer resistance (R_{ct}). The curve fit analysis of these electrochemical impedance spectroscopy (EIS) data is provided in Fig. S5 and Table S2 (ESI†). When Sn is incorporated with x = 0.1, the charge transfer resistance is much larger than that of GeS (x = 0). In contrast, the composition x = 0.8 possesses the lower charge transfer resistance than SnS. These results suggest that the incorporation of Ge into SnS induces the higher diffusivity of Li^+ ions and decreases their charge transfer resistance. As we discussed earlier, this composition could have the higher electrical conductivity. Overall, therefore, the excellent rate capability of the higher Sn compositions can be attributed to their high electrical and ionic conductivities.

After a few cycles, all $Sn_xGe_{1-x}S$ NCs are completely decomposed into Sn_xGe_{1-x} NCs. Therefore, the reversible capacities are actually determined by the lithiation/delithiation processes of Sn_xGe_{1-x} NCs. It has been reported that the diffusion rate of Li ions in bulk Sn ($2–6\times10^{-7}$ cm^2 s^{-1} at 25 °C) is higher than in Ge (3.1×10^{-9} cm^2 s^{-1} at 150 °C).[3,35] As x increases, the faster Li^+ ion diffusion rate would, therefore, enable the higher rate capability to be maintained. Consequently, we may simply rationalize that the higher rate capability of the Sn-rich alloy NCs is due to their higher Li^+ ion diffusion rates. However, our previous work revealed the phase conversion of Ge and Sn NCs, following their irreversible production from GeS and SnS NCs, respectively.[7,24] Accordingly, we need to explain these results more carefully using the phases underlying the lithiation/delithiation processes.

For GeS NCs, metastable tetragonal (ST12) phase Ge has been observed to be produced upon lithiation and became the dominant phase after a few cycles.[6,7] This ST12 Ge undergoes significant amorphization due to its large volume change. In the case of SnS NCs, tetragonal phase Sn (β-Sn) has been observed to be initially produced by an irreversible decomposition step.[24] As the cycle number increases, a diamond-type cubic Sn (α-Sn) phase is produced and becomes the dominant phase because it suffers a smaller volume change upon lithiation/delithiation. We monitored the *ex situ* XRD patterns for compositions x = 0, 0.1, 0.4, 0.8, and 1 after 70 cycles, as shown in the ESI†, Fig. S6. The results confirm the production of cubic phase $Sn_{1-x}Ge_x$ alloy NCs when x = 0.8 and 1. Therefore, the persistence of the crystalline Sn-Ge alloy NCs may decrease the charge transfer resistance maintaining the reversible lithiation/delithiation processes, and consequently, allow for the larger observed rate capability. Nevertheless, this needs more investigation to support our model. The present results will contribute to the development of new Sn-based materials that have higher capacities at higher C rates.

Conclusions

$Sn_xGe_{1-x}S$ ($0 \le x \le 1$) ternary alloy NCs were synthesized by a gas-phase laser photolysis reaction of a TMG, TMT, and H_2S mixture in a closed reactor. Complete composition control was achieved using the partial pressure of the precursors. All the resulting composition-tuned NCs consisted of a high-purity orthorhombic phase and showed excellent cycling performance in LIBs. The reversible capacities were in the range 800–1200 mAh/g (at 0.1C) after 70 cycles, which is close to the theoretical value of bulk $Ge_{1-x}Sn_x$. Rate capabilities were tested by increasing the C rate up to 5C, showing the greatest enhancement for the Sn-rich composition. A lower Li^+ ion charge transfer resistance was also observed at the Sn-rich alloy composition (by Nyquist plots). This unique composition dependence of the $Sn_xGe_{1-x}S$ NCs is remarkably consistent with their photoconversion efficiency in photovoltaic devices. The excellent electrochemical properties of the Sn-rich compositions could be ascribed to the higher electrical and ionic conductivities of $Sn_xGe_{1-x}S$ as well as Sn_xGe_{1-x} alloy NCs. We also suggest the possibility that the production and persistence of the crystalline cubic phase $Sn_{1-x}Ge_x$ alloy NCs upon lithiation could lower the charge transfer resistance. Sn-rich $Sn_xGe_{1-x}S$ NCs are, therefore, promising candidates for applications in high-performance energy conversion systems.

Acknowledgements

This study was supported by Hoseo University. The HVEM (Daejeon) and XPS (Pusan) measurements were performed at the KBSI. The experiments at the PLS were partially supported by MOST and POSTECH.

Notes and references

[a] Department of Chemistry, Korea University, Jochiwon 339-700, Korea.
[b] Department of Pharmaceutical engineering, Hoseo university, Hoseo University, Chungnam 336-795, Korea.
[c] Center for Energy Convergence, Korea Institute of Science and Technology, Seoul 136-791, Korea.
*Corresponding Authors: parkjh@korea.ac.kr; chaeunhee@hoseo.edu; wonic@kist.re.kr

† Electronic supplementary information (ESI) available: [Fig. S1-S6. Lattice parameters, band gap, CV data, differential voltage profiles, ESI data, and XRD pattern of discharged LIB electrode]. See DOI: 10.1039/b000000x/

1 M. R. St. John, A. J. Furgala and A. F. Sammells, *J. Electrochem. Soc.*, 1982, **129**, 246.
2 J. Graetz, C. C. Ahn, R. Yazami and B. Fultz, *J. Electrochem. Soc.*, 2004, **151**, A698.
3 R. A, Higgns, *J. Power Sources*, 1999, **81-82**, 13.
4 M. Winter and J. O. Besenhard, *Electrochim. Acta*, 1999, **45**, 31.
5 Y. Kim, H. Hwang, K. Lawler, S. W. Martin and J. Cho, *Electrochim. Acta*, 2008, **53**, 5058.

6 Y. J. Cho, H. S. Lim, C. H, Kim, H. S. Kim, S. H. Back, Y. L. Lim, C. S. Jung, D. M. Jang, J. Park, E. H. Cha, M. S. Song and W. I. Cho, *Chem. Commun.*, 2013, **49**, 4661.
7 Y. J. Cho, H. S. Im, H. S. Kim, Y. Myung, S. H. Back, Y. R. Lim, C. S. Jung, D. M. Jang, J. Park, E. H. Cha, W. I. Cho, F. Shojaei and H. S. Kang, *ACS Nano*, 2013, **7**, 9075.
8 T. -J. Kim, C. Kim, D. Son, M. Choi and B. Park, *J. Power Sources*, 2007, **167**, 529.
9 J. -W. Seo, J. -T. Jang, S. -W. Park, C. Kim, B. Park and J. Cheon, *Adv. Mater.*, 2008, **20**, 4269.
10 C. Zhai, N. Du, H. Zhang, J. Yu, and D. Yang, *ACS Appl. Mater. Interfaces*, 2011, **3**, 4067.
11 J. Zai, K. Wang, Y. Su, X, Qian and J. Chen, *J. Power Sources*, 2011, **196**, 3650.
12 Y. Zhang, J. Lu, S. Shen, H. Xu and Q. Wang, *Chem. Commun.*, 2011, **47**, 5226.
13 K. Chang, Z. Wang, G. Huang, H. Li , W. Chen and J. Y. Lee, *J. Power Sources*, 2012, **201**, 259.
14 P. Wu, N. Du, H. Zhang, J. Liu, L. Chang, L. Wang, D. Yang and J. Z. Jian, *Nanoscale*, 2012, **4**, 4002.
15 D. D. Vaughn II, O. D. Hentz, S. Chen, D. Wang and R. E. Schaak, *Chem. Commun.*, 2012, **48**, 5608.
16 Z. Jiang, C. Wang, G. Du, Y. J. Zhong and J. Z. Jiang, *J. Mater. Chem.*, 2012, **22**, 9494.
17 M. Zhang, D. Lei, X. Yu, L. Chen, Q. Li, Y. Wang, T. Wang and G. Cao, *J. Mater. Chem.*, 2012, **22**, 23091.
18 J. Yin, H. Cao, Z. Zhou, J. Zhang and M. Qu, *J. Mater. Chem.*, 2012, **22**, 23963.
19 M. Sathish, S. Mitani, T. Tomai and I. Honma, *J. Phys. Chem. C*, 2012, **116**, 12475.
20 Y. Du, Z. Yin, X. Rui, Z. Zeng, X. -J. Wu, J. Liu, Y. Zhu, J. Zhu, X. Huang, Q. Yan and H. Zhang, *Nanoscale*, 2013, **5**, 1456.
21 Q. Wu, L. Jiao, J. Du, J. Yang, L. Guo, Y. Liu, Y. Wang and H. Yuan, *J. Power Sources*, 2013, **239**, 89.
22 X. Jiang, X. Yang, Y. Zhu, J. Shen, K. Fan, and C. Li, *J. Power Sources*, 2013, **237**, 178.
23 S. Liu, X. Lu, J. Xie, G. Cao, T. Zhu and X. Zhao, *ACS Appl. Mater. Interfaces*, 2013, **5**, 1588.
24 H. S. Im, Y. J. Cho, Y. R. Lim, C. S. Jung, D. M. Jang, J. Park, F. Shojaei and H. S. Kang, *ACS Nano*, 2013, **7**, 9075.
25 S. H. Choi and Y. C. Kang, *Small,* 2014, **10***,* 474.
26 D. D. Vaughn II, R. J. Patel, M. A. Hickner and R. E. Schaak, *J. Am. Chem. Soc.*, 2010, **132**, 15170.
27 S. G. Hickey, C. Waurisch, B. Rellinghaus, and A. Eychmüller, *J. Am. Chem. Soc.*, 2008, **130**, 14978.
28 Y. Wang, H. Gong, B. Fan and G. Hu, *J. Phys. Chem. C*, 2010, **114**, 3256.
29 J. Chao, Z. Xie, X. B. Duan, Y. Dong, Z. Wang, J. Xu, B. Liang, B. Shan, J. Ye, D. Chen and G. Shen, *CrystEngComm*, 2012, **14**, 3163.
30 Z. Deng, D. Cao, J. He, S. Lin, S. M. Lindsay and Y. Liu, *ACS Nano*, 2012, **6**, 6197.
31 J. Chao, Z. Wang, X. Xu, Q. Xiang, W. Song, G. Chen, J. Hu and D. Chen, *RSC Adv.*, 2013, **3**, 2746.
32 M. Steichen, R. Djemour, L. Gütay, J. Guillot, S. Siebentritt and P. J. Dale, *J. Phys. Chem. C*, 2013, **117**, 4383.
33 X. Liu, B. Zhou, X. Wang, A. N. Cartwright and M. T. Swihart, *Chem. Mater.*, 2014, **26**, 3515.
34 H. S. Im, Y. Myung, K. Park, C. S. Jung, Y. R. Lim, D. M. Jang and J. Park, *RSC Adv.*, 2014, **4**, 15695.
35 C. S. Fuller and J. C. Severiens, *Phys. Rev.*, 1954, **96**, 21.

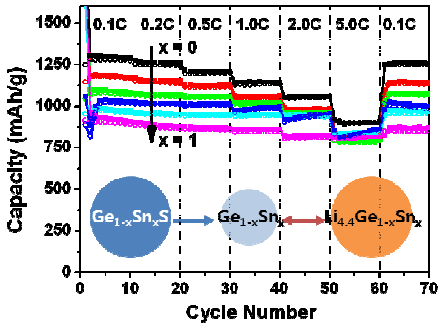

Complete composition-tuned $Sn_xGe_{1-x}S$ alloy nanocrystals exhibit excellent cycling performances in lithium ion batteries, with the greatest rate capability for Sn-rich compositions.